Air-propelled, herringbone-textured platelets

Hélène de Maleprade,[1,2,3] Dan Soto,[1,2] David Quéré,[1,2] E. John Hinch,[3] Tobias Baier,[4]
Maximilian T. Schür,[4] and Steffen Hardt[4]

[1]*Physique & Mécanique des Milieux Hétérogènes, UMR 7636 du CNRS, ESPCI, 75005 Paris, France*
[2]*Ladhyx, UMR 7646 du CNRS, École polytechnique, 91128 Palaiseau Cedex, France*
[3]*Department of Applied Mathematics and Theoretical Physics, Centre for Mathematical Sciences,*
University of Cambridge, Cambridge CB3 0WA, United Kingdom
[4]*Institute for Nano- and Microfluidics, Technische Universität Darmstadt,*
Alarich-Weiss-Straße 10, 64287 Darmstadt, Germany

Solids can be levitated by actively nourishing an air cushion beneath them, using air blown through a porous substrate. It has recently been demonstrated that introducing asymmetry in the airflow close to a hovercraft can lead to its propulsion by viscous entrainment. In this work, we focus on the major consequence of a simple modification in the set-up: instead of engraving the texture on the substrate as in previous works, we directly carve it into the hovercraft. Provided that air-flux is strong enough, propulsion at any Reynolds number is observed. However, motion happens in the direction opposite to the viscous scenario. To understand experimental observations, an analytical model is proposed to account for the force of propulsion and the pressure needed for levitation, emphasizing asymptotic situations at low and high Reynolds numbers, further confirmed by numerical simulations.

I. INTRODUCTION

Flying is one of the oldest human dreams that has stimulated imagination from arts and literature to engineering. Here we discuss a modern version of the magic carpet described about 1300 years ago in the *Arabian Nights*. Levitation of the "carpet" can be achieved by various techniques [1] ranging from heat [2], acoustics [3], or magnetism [4] to optics [5] and aerodynamics [6–9]. Besides, we also seek propulsion, and recent works in the Leidenfrost situation [10,11] offer new ways to control it: A hot ratchet [12] does not only allow levitation but it also induces propulsion. Pressed by the levitating object, vapor beneath it is evacuated along the teeth of the ratchet and drags the object by viscosity [13]. This concept has been further developed in a geometry where grooves are displayed in a herringbone design, and vapor has no other option than following the asymmetrical channel pattern [14], so that the vapor and the object move along the same direction. The use of heat to induce levitation can be circumvented by blowing air through the structure, using a porous substrate [6–9,15–17]. Similarly, if a herringbone texture is present on the porous substrate [7] as illustrated in Fig. 1(a), motion arises again in the same direction as air flow, that is, opposing the direction pointed by the chevrons.

The latter device offers contactless manipulation of objects, useful to avoid deterioration by contamination or shock; however, it faces severe limitations. Indeed, this set-up forces us to texture the whole air-blowing substrate. Apart from being costly and technically challenging, a fixed design imposes both the trajectory and the speed of hovercrafts; moreover, it prevents the simultaneous propulsion of different solids. Hence, the idea to work with a flat porous substrate and to texture only the bottom side of the levitating platelet. This minor modification changes the propulsion mechanism dramatically, as seen in Fig. 1(b) and Supplemental Material movie 1 [18], where we observe that the direction of motion is reversed compared to the previous case [Fig. 1(a)]. The aim of this work is to
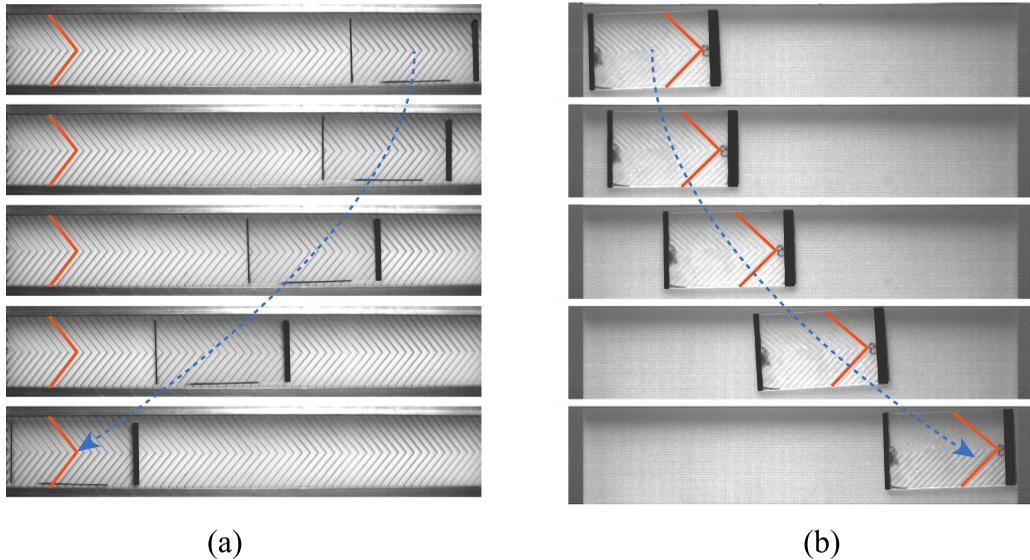
(a)   (b)

FIG. 1. Image sequences showing trajectories of levitating plates; time between pictures is 0.5 s. Hovercrafts are 30 mm long and 160 μm thick; their velocity is null in the top picture. A herringbone texture (highlighted by orange lines) is engraved either on the substrate (a) or on the levitating object (b). Patterns are identically oriented, but the motion of the hovercraft takes place in opposite directions. Blue arrows show the movement of the center of mass of the plates. Typical final speeds are around 6 cm/s in both cases.

understand this surprising effect and more generally to establish the principles of levitating platelets propulsion. We propose an analytical description of the phenomenon, focusing first on the analysis of the propelling force and also on the pressure needed to induce levitation, two key quantities in our system. The analytical model highlights two asymptotic regimes depending on the Reynolds number and the channel geometry, which we discuss and confirm by experiments and numerical simulations.

II. EXPERIMENT DESCRIPTION

The set-up used for the experiments shown in Fig. 1(b) is illustrated in Fig. 2. A glass slide with length $a = 30$ mm, width $b \in [6, 12, 18, 24]$ mm, and thickness $c \in [160, 1160, 2160]$ μm displays on its bottom a herringbone texture with opening angle $2\alpha = 90°$ made of channels with width $w = 1$ mm separated by thin walls with thickness $\lambda = 200 \, \mu$m and height $h \in [150, 250, 400, 800, 1600] \, \mu$m. Channels have a length $l = b/(2\sin\alpha)$. Hovercrafts are created by sticking textures made of reticulated glue on a glass slide. Further details on this process can be found in the Supplemental Material [18].

A typical experiment consists of placing this object on top of a Plexiglass box, whose porous cover (thickness $e = 2$ mm) has pores with radius $r = 90 \pm 10 \, \mu$m and mutual distance $d = 400 \, \mu$m. The overpressure P_2 inside the box, larger than the atmospheric pressure P_0, is carefully increased (and controlled using a testo-510 manometer) until the plate starts levitating. The induced airflow [blue arrows, Fig. 2(a)] is subsequently channeled in the herringbone grooves [red arrows, Fig. 2(b)]. Air velocity is locally described by its horizontal component u in the x-direction (along the channel) and by its vertical component v. This flow is associated to an overpressure p inside the grooves, which results in the plate movement in the X-direction [yellow arrow in Fig. 2(b)] with a velocity V.

By recording the motion with a video-camera (uEye SE, 50 frames per second), we access the plate position as a function of time, visible in Fig. 1(b) and Supplemental Material movie 1 [18]. The parabolic trend, underlined by the blue arrow, is characteristic of a frictionless state. To measure
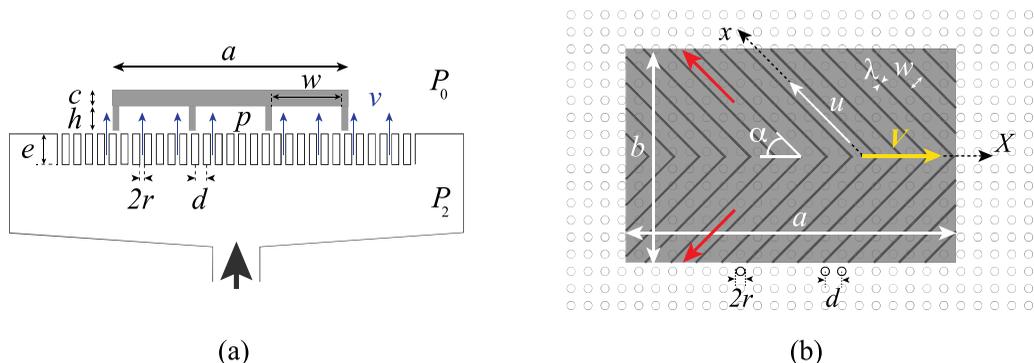
(a)

(b)

FIG. 2. (a) Side and (b) top view of the set-up. An overpressure P_2 above atmospheric pressure P_0 is imposed in a Plexiglas box whose porous top has holes with radius r, spacing d, and length e. Air flows through the pores (blue arrows) and interacts with a textured glass plate (length a, width b, and thickness c). The bottom side of the plate is made of channels arranged in a herringbone design (opening angle 2α, height h, and thickness λ spaced by w), in which the overpressure is p. Air velocity at a position x in a channel has horizontal and vertical components, u and v. After being redirected by the channels, air escapes in the direction pointed by the red arrows. Propulsion of the slider at a velocity V (yellow arrow) happens in the opposite direction.

the driving force, the hovercraft is launched several times against the propelling direction (velocity $V_0 \approx -8$ cm/s). The plate slows down, stops, and accelerates in the opposite direction to reach about $V \approx 6$ cm/s at the end of the 10-cm-long track. Acceleration is measured around the turning point, when the plate changes its direction, by fitting the position as a function of time with a parabola. The force F is deduced by multiplying this acceleration with the mass of the plate, in a problem where the input parameters are the slider geometry and the overpressure P_2 chosen by the operator.

When airflow and hovercraft motion happen in the same direction [Fig. 1(a)], it has been shown that viscous drag on the underside of the slide is responsible for the propulsion [7]. Here, grooves are imprinted onto the slider so that the pressure profile within each groove imparts an additional force on their sidewalls, which tends to push the slider in the spine direction while the viscous drag tends to drive it in the opposite direction. We discuss in this paper the amplitude of these conflicting forces, which allows us to understand the observed motion and its surprising direction. We first develop an analytical model based on an analysis of the airflow at the channel level. Then we test this model with a series of original experiments and simulations where we vary the geometrical characteristics of the slider. It is shown that the hovercraft speed can be controlled by playing on these parameters, which produces a simple, versatile and mobile device that can be used on flat substrates.

III. PROBLEM STATEMENT

For a simplified description of the flow in a shallow groove of length l and height h, assumed to be much smaller than its width w, we neglect the influence of the sidewalls and consider a two-dimensional geometry. Air enters each channel at the position $y = 0$ and flows toward the exit located at $x = l$, where $l = b/(2\sin\alpha)$ is the channel length, as sketched in Fig. 3. The origin of x is taken at the center of the slide, corresponding to the tip of the herringbone. To evaluate the propulsion force F and the working pressure P_2, we have to describe the evolution of the pressure and flow profiles along the channel.

A. Governing equations

We consider an incompressible two-dimensional flow with velocity components $u(x, y)$, $v(x, y)$ and pressure $p(x, y)$. Focusing on the steady-state regime, the governing equations for an
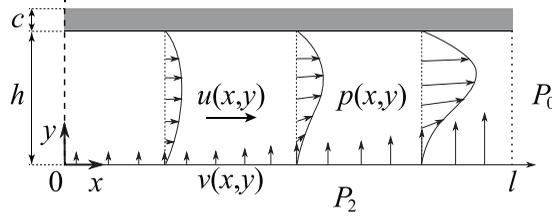
FIG. 3. Cross-section of the channel domain used in the model. Flow happens below the solid of thickness c in a volume of height h and length $l = b/(2\sin\alpha)$. The horizontal velocity of air is $u(x, y)$ and the vertical velocity is $v(x, y)$. The overpressure in the reservoir is P_2 and inside the channel is $p(x, y)$, larger than the atmospheric pressure P_0.

inertial flow in a long and thin channel, $h \ll l$, are

$$u_x + v_y = 0, \tag{1a}$$

$$\rho(uu_x + vu_y) = -p_x + \eta(u_{xx} + u_{yy}), \tag{1b}$$

$$\rho(uv_x + vv_y) = -p_y + \eta(v_{xx} + v_{yy}), \tag{1c}$$

with the viscosity η and density ρ of air and a subscript denoting the partial derivative with respect to the corresponding coordinate.

B. Boundary conditions

The horizontal velocity has to satisfy no-slip boundary conditions at the bottom and the top of the channel. Besides, due to symmetry, there is no flow at the closed end of the channel:

$$u(x, 0) = 0, \quad u(x, h) = 0, \quad \text{and} \quad u(0, y) = 0. \tag{2a}$$

The bottom flux through the porous cover of permeability $k = \pi r^4/(8d^2 e)$ is governed by the pressure difference between the reservoir and the channel, while the vertical velocity satisfies no flux through the top:

$$v(x, 0) = \frac{k}{\eta}(P_2 - p), \quad \text{and} \quad v(x, h) = 0. \tag{2b}$$

Moreover, pressure continuity at the open end of the channel yields

$$p(l) = P_0. \tag{2c}$$

C. Forces

With these governing equations and boundary conditions, we aim at capturing the flow profile evolution along the channel and evaluating various forces: the horizontal force F_p generated by the overpressure at the tip, the horizontal viscous forces on the top and bottom boundaries F_t and F_b, and the vertical force F_g enabling levitation. These forces per unit length are given by

$$\mathbf{F}_p \equiv F_p\hat{\mathbf{x}} = \int_0^h \{-(\mathbf{T} \cdot \mathbf{n})|_{x=0} \cdot \hat{\mathbf{x}} + P_0\}dy \, \hat{\mathbf{x}} = [P_0 - p(0)]h \, \hat{\mathbf{x}},$$

$$\mathbf{F}_t \equiv F_t\hat{\mathbf{x}} = \int_0^l \{-(\mathbf{T} \cdot \mathbf{n})|_{y=h} \cdot \hat{\mathbf{x}}\}dx \, \hat{\mathbf{x}} = \int_0^l -\eta \, u_y(x, h)dx \, \hat{\mathbf{x}},$$

$$\mathbf{F}_b \equiv F_b\hat{\mathbf{x}} = \int_0^l \{-(\mathbf{T}\cdot\mathbf{n})|_{\boldsymbol{y}=0}\cdot\hat{\mathbf{x}}\}dx\,\hat{\mathbf{x}} = \int_0^l \eta\,u_y(x,0)dx\,\hat{\mathbf{x}},$$

$$\mathbf{F}_g \equiv F_g\hat{\mathbf{y}} = \int_0^l \{-(\mathbf{T}\cdot\mathbf{n})|_{\boldsymbol{y}=h}\cdot\hat{\mathbf{y}} - P_0\}dx\,\hat{\mathbf{y}} = \int_0^l [p(x) - P_0]dx\,\hat{\mathbf{y}}, \tag{3}$$

where $\mathbf{T}$ denotes the stress tensor. The normal vector $\mathbf{n}$ points outward of the fluid domain, while $\hat{\mathbf{x}}$ and $\hat{\mathbf{y}}$ are unit vectors pointing in the respective coordinate directions.

The net propulsion force in a single channel is $F_p + F_t$, as these two forces apply on the textured walls connected to the levitating object. F_b applies to the porous substrate, assumed to be immobile in the experiments we want to describe. The global horizontal momentum balance inside the channel takes into account the momentum flux out of the channel, so that

$$F_p + F_t + F_b + \int_0^h \rho u^2(l, y)dy = 0.$$

The viscous stress contribution at the outlet is negligible compared to the convective momentum transport and has been omitted in the balance. Since the last two terms are positive, the net propulsion force due to each channel on the slider, $F_p + F_t$, acts in opposite direction of the flow.

D. Nondimensionalization

To nondimensionalize the equations, we scale x and y by the characteristic horizontal and vertical lengths l and h, respectively, and $(p - P_0)$ by the pressure $(P_2 - P_0)$. Defining $v_m = \frac{k}{\eta}(P_2 - P_0)$, the maximum influx across the porous plate, we scale the time t by h/v_m and the horizontal and vertical components of the velocity, u and v, by $\frac{l}{h}v_m$ and v_m, respectively. Governing Eqs. (1) then become

$$u_x + v_y = 0, \tag{1a$'$}$$

$$\mathrm{Re}(uu_x + vu_y) = -Kp_x + (\varepsilon^2 u_{xx} + u_{yy}), \tag{1b$'$}$$

$$\varepsilon^2\mathrm{Re}(uv_x + vv_y) = -Kp_y + \varepsilon^2(\varepsilon^2 v_{xx} + v_{yy}), \tag{1c$'$}$$

where $\varepsilon = h/l \ll 1$ and we introduced two nondimensional parameters playing a key-role in our study, namely, the Reynolds number Re and K, the ratio of pressure drop across the porous plate by the pressure drop down the channel:

$$\mathrm{Re} = \frac{\rho v_m h}{\eta}, \tag{4a}$$

$$K = \frac{h^3}{kl^2} = \varepsilon^2\frac{h}{k}. \tag{4b}$$

These parameters are directly related to the experimental conditions. Indeed, the Reynolds number $\mathrm{Re} = \rho k(P_2 - P_0)/\eta^2$ is proportional to $P_2 - P_0$, the pressure inside the box chosen by the operator to observe levitation. The ratio K strongly depends on the geometry of the channel, its height h, and length l being varied throughout the study. Since in our experiments $\varepsilon \ll 1$ and $h/k \gg 1$, in particular, $K \gg \max(\varepsilon^2\mathrm{Re}, \varepsilon^2)$, Eq. (1c$'$) establishes that to a good approximation the pressure is independent of y, such that $p(x, y)$ reduces to $p(x)$, and the contribution of u_{xx} to the viscous term in Eq. (1b$'$) can be neglected, recovering the lubrication approximation in a narrow gap.

Regarding the boundary conditions, Eqs. (2a) and (2b) remain null, while the flow through the porous plate Eq. (2b) and the pressure continuity Eq. (2c) at the open end of the channel become

$$v(x, 0) = 1 - p, \tag{2b$'$}$$

$$p(1) = 0. \tag{2c$'$}$$

Horizontal forces are scaled by $(P_2 - P_0)h$ while the vertical one is scaled by $(P_2 - P_0)l$, leading to

$$F_p = -p(0), \quad F_g = \int_0^1 p(x)dx, \quad F_t = -\frac{1}{K}\int_0^1 u_y(x, 1)dx, \tag{3'}$$

$$F_b = \frac{1}{K}\int_0^1 u_y(x, 0)dx.$$

Here we confirm the importance of the ratio K, which together with the Reynolds number Re will govern the propulsion and regulate the interplay between forces. Depending on the Reynolds number (high or low) and on the channel geometry (long or short channels corresponding to $K \ll 1$ and $K \gg 1$, respectively), several asymptotic cases arise.

IV. ASYMPTOTIC REGIMES

A. High Reynolds numbers

In the case of high Reynolds numbers, the viscous terms in the momentum Eq. (1b′) can be neglected, leading to $\mathrm{Re}(uu_x + vu_y) = -K p_x$. In this limit, we expect the velocity profile to only change weakly along the channel, such that the inviscid flow has a separable solution:

$$u(x, y) = -f(x)g'(y), \quad v(x, y) = f'(x)g(y), \tag{5}$$

where g' can be interpreted as the velocity profile while f' is the influx velocity over the porous wall, fixing a first boundary condition, $g(0) = 1$. Substituting the solutions for u and v in Eq. (1b′) yields

$$\mathrm{Re}(ff'g'^2 - ff'gg'') = -K p_x. \tag{1b''}$$

Equation (1b″) can be rewritten as $g'^2 - gg'' = -K p_x/(\mathrm{Re} ff')$, so that the left and right terms are both functions of y and x only. Hence both sides are constant, equal to a^2. The equation $g'^2 - gg'' = a^2$ together with the boundary condition $g(0) = 1$ and the ones implemented from (2), no flux through the top $g(1) = 0$ and no slip on the porous plate $g'(0) = 0$, has a solution for $a = \pi/2$, which is $g(y) = \cos(\pi y/2)$. This velocity profile also shows a vorticity $u_y - \varepsilon^2 v_x$ that is constant along streamlines to lowest order in ε. As viscous terms are neglected, the no-slip boundary condition on the top at $y = 1$ cannot be demanded anymore. This slip calls for a boundary layer, for which the solution is not separable; details of this correction to the main flow are given in Appendix A. By integrating (1b″) with respect to x, we obtain a Bernoulli type equation:

$$\beta^2 f^2(x) + p(x) = p(0), \quad \text{with } \beta^2 = \frac{a^2}{2}\frac{\mathrm{Re}}{K} = \frac{\pi^2}{8}\frac{\mathrm{Re}}{K}, \tag{6}$$

where $p(0)$ is the unknown pressure at the tip of the herringbone, and we introduced the parameter β. The inflow condition (2b′) yields $f'(x) = 1 - p(x)$, so that we get $f'(x) = 1 - p(0) + \beta^2 f^2(x)$. This differential equation can be integrated into

$$f(x) = \frac{\sqrt{1 - p(0)}}{\beta}\tan(\sqrt{1 - p(0)}\beta x). \tag{7}$$

The pressure $p(0)$ is determined by the continuity of pressure at the exit of the channel, $p(1) = 0$, expressed here as $\beta^2 f^2(1) = p(0)$:

$$\tan^2(\sqrt{1 - p(0)}\beta) = \frac{p(0)}{1 - p(0)}. \tag{8}$$

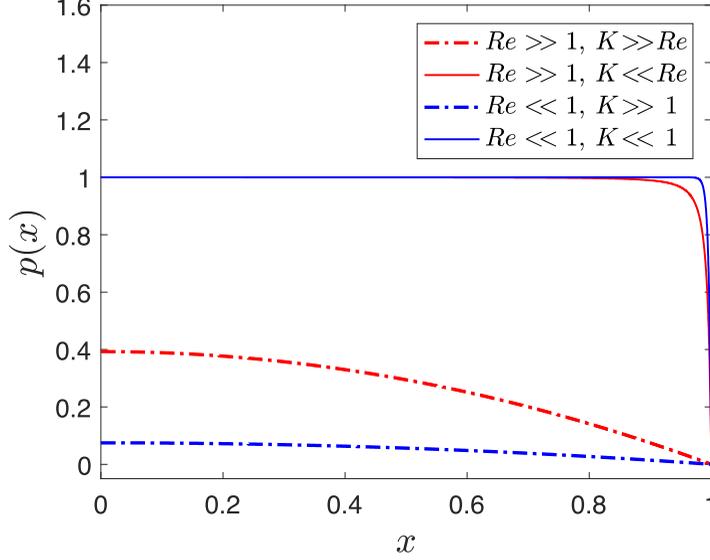To solve for the high Reynolds numbers limit, we now focus on the two limits defined by the channel length.

FIG. 4. Channel pressure p as a function of the position x. High Reynolds asymptotic cases are plotted in red, while low Reynolds cases are in blue. Dashed lines stand for short channels, while solid lines correspond to long channels. The values chosen for this graph are the minimum and maximum numerical Reynolds numbers (0.25–295), corresponding to the minimum and maximum values of K (0.05–927) for our experiments. Only for Re $\ll 1$ and $K \gg 1$ (blue dashed line), we used $K = 30$ to emphasise the nonzero and nonmonotonic behavior of the pressure.

1. Short channels, $K \gg Re$

For short channels, most of the pressure drop occurs across the porous plate. Thus, to a first order, we expect no variation along the channel, and $p(x) \approx 0$ for $0 < x < 1$, leading to a uniform flow across the plate, $v(x, 0) \approx 1$. In this limit, corresponding to a large influx into the channel, using Eq. (8) and $\beta \ll 1$ we get $p(0) \approx \beta^2$. Replacing this in Eq. (6), the pressure can be approximated by $p(x) \approx \beta^2(1 - x^2)$, that is a quadratic correction to the zero pressure in the channel, plotted in Fig. 4. Equation ((3′)) yields the forces

$$F_p = -\frac{\pi^2}{8}\frac{Re}{K}, \quad F_t = O(Re^{1/2}/K), \quad F_b = O(1/K), \quad F_g = \frac{\pi^2}{12}\frac{Re}{K}, \tag{9}$$

where we used the boundary layer correction (described in Appendix A) on the top surface to establish the dependency of F_t.

2. Long channels, $Re \gg K$

For long channels, most of the pressure drop occurs down the channel, near the exit. We thus expect much of the channel to be at the pressure below the porous plate: $p(x) \approx 1$, for all x, except just near $x = 1$. From the inflow condition (2b′) and Eq. (6), we had $f'(x) = 1 - p(0) + \beta^2 f^2(x)$, which for long channels, as $\beta \gg 1$, yields $f'(x) \approx \beta^2 f^2(x)$. The maximal influx velocity at the exit of the channel (2′) gives the boundary condition $f'(1) = 1$ and thus $f(x) \approx \frac{1/\beta^2}{1/\beta + 1 - x}$. The pressure inferred from Eq. (6) is $p(x) \approx 1 - \beta^2 f^2(x)$. Hence, there is a small region of $x = 1 - O(\sqrt{K/Re})$, where the pressure drops from the central value of $p(0) \approx 1$ to the value at the exit $p(1) = 0$. More specifically, as $1 - p(0)$ is small, Eq. (8) demands $\sqrt{1 - p(0)}\beta \approx \pi/2$, or $p(0) \approx 1 - \pi^2/(2\beta)^2$,

and we have the forces

$$F_p = -1 + 2\frac{K}{\text{Re}}, \quad F_t = O(\text{Re}^{-1/2}), \quad F_b = O(\text{Re}^{-1}), \quad \text{and} \quad F_g = 1 - \sqrt{\frac{8}{\pi^2}\frac{K}{\text{Re}}}. \tag{10}$$

In both short and long channel situations, the resulting forces Eqs. (9) and (10) logically show a negligible influence of the viscous components, F_t and F_b. In this high Reynolds number limit, the total propulsion $F_p + F_t$ originates from pressure effects and results in only F_p. Note that since for long channels the flow is confined to a small region $\Delta x \sim O(\sqrt{K/\text{Re}}) \ll 1$ at the end of the channel, the restriction imposed on K for the lubrication approximation to be valid should be based on Δx instead of the full channel length l. Similarly, a separable solution of the form of Eq. (5) is only adequate in this region, cf. Appendix B. However, since F_p and F_g are dominated by the uniform pressure beneath most of the plate and only receive a small correction due to the details of the flow at the outlet, Eq. (10) remains an excellent approximation regardless.

B. Low Reynolds numbers

For low Reynolds numbers, a detailed derivation can be found in Ref. [7], so that we only present here the main results. Standard lubrication theory and mass conservation yields the volume flux conditions $q = -\frac{K}{12}p_x$ and $q_x = v = 1 - p$ (the first equation results from the integration of (1b′) for Re $\ll 1$, $0 = -Kp_x + u_{yy}$). Combining them, we get a second-order differential equation, $-\frac{K}{12}p_{xx} = 1 - p$, with solution $p(x) = 1 - \frac{\cosh x/\sigma}{\cosh 1/\sigma}$, where $\sigma = \sqrt{K/12}$ is the characteristic horizontal length scale. This gives the forces

$$F_p = -1 + \text{sech}(1/\sigma), \quad F_t = F_b = -F_p/2, \quad \text{and} \quad F_g = 1 - \sigma \tanh(1/\sigma).$$

In this low Reynolds numbers case, regardless of the channel length, we always have a viscous contribution that is not negligible anymore (compared to the previous case of Re $\gg 1$), and that lowers the pressure contribution to the propulsion by half, $F_t = -F_p/2$. This explains the surprising observations in Fig. 1. When the textures are on the slider, then the total propulsive force is $F_p + F_t = F_p/2$. In contrast, for a texture engraved on the porous box, the propulsion becomes $0 + F_t = -F_p/2$, as the contribution of the pressure vanishes (it applies on the fixed walls of the box) [7], justifying the opposite direction of movement.

More specifically, in the short channel limit we again expect no pressure variation as for large Re. Indeed, for $K \gg 1$, $p(x) \ll 1$ for $0 < x < 1$, as seen in Fig. 4. We get the following forces

$$F_p = -6/K, \quad F_t = F_b = 3/K, \quad F_g = 4/K, \tag{11}$$

while in the long channel limit, $K \ll 1$, one finds that there is a small region of $x = 1 - O(K^{1/2})$, where the pressure drops from the central value of $p(0) = 1$ to the value at the exit $p(1) = 0$. This leads to the forces

$$F_p = -1 + 2e^{-\sqrt{12/K}}, \quad F_t = F_b = 1/2 + e^{-\sqrt{12/K}}, \quad \text{and} \quad F_g = 1 - (K/12)^{1/2}. \tag{12}$$

V. DISCUSSION

A. Channel pressure profile

We can now describe the pressure inside the channel, as obtained in the asymptotic cases. This is shown in Fig. 4, where we notice that for long channels (solid lines), the pressure profile does

not depend on the Reynolds number. It is nearly constant and equal to unity, with a small region near the end where the pressure drops down to zero. Conversely, short channels (dashed lines) show a parabolic pressure profile. For long channels at low Reynolds numbers, the pressure variation is small, in $O(1/K)$, hardly visible in Fig. 4. In the corresponding high Reynolds number limit, the variation remains small, yet larger, in $O(\text{Re}/K)$.

B. Force ratio

Now that we have derived equations to describe the flow profile evolution along the channel and various forces, we transpose these results into observable physical parameters, namely, the total propelling force F and the pressure P_2 needed to observe levitation of the slider. The force of propulsion applied on the slider in a single channel arises from the contribution of the pressure F_p acting on the walls and the viscosity F_t acting on the top of the channel (i.e., on the bottom of the slider). It varies from $F_p/2$ to F_p as the Reynolds number increases. Moreover, the force of levitation in a channel F_g varies between $2F_p/3$ for short channels and F_p for long channels. Each channel contributes $F = (F_p + F_t)\cos\alpha$ to the total propulsion force on the plate, where the $\cos\alpha$ originates from the projection of a single channel on the direction of motion. Returning to dimensional quantities, the ratio between the forces of propulsion and levitation is

$$F/F_g = -\delta(h/l)\cos\alpha, \quad \text{with } \delta = \begin{cases} 1/2, & \text{Re} \ll 1, & K \ll 1 \\ 3/4, & \text{Re} \ll 1, & K \gg 1 \\ 1, & \text{Re} \gg 1, & K \ll \text{Re} \\ 3/2, & \text{Re} \gg 1, & K \gg \text{Re} \end{cases}. \tag{13}$$

The force of propulsion F scales as the levitation force F_g, chosen to compensate the weight, and depends on the slenderness $\varepsilon = h/l$ of the channel. The force ratio is always smaller than 1, as it compares the pressure applied to the small area hw at the end of the channel with the same pressure (within a factor δ) applied to the large area lw of the top surface. The numerical coefficient δ is described by this equation to be bounded between $1/2$ and $3/2$. Although these values are all close to 1, the total propelling force intensity can be tripled depending on the Reynolds number and geometry of the slider.

Experimental results are compared to this theoretical prediction in Fig. 5(a), where the measured propelling force (normalized by the platelet weight) is plotted as a function of the geometrical parameter $(h/l)\cos\alpha$. Besides collapsing to a narrow band and showing a fair agreement, our data are slightly lower than expected, especially at large or very small Re. In both cases, small losses of efficiency in the propulsion can arise from solid friction between the texture and the substrate, leakage between channels, the drag of air at the top of the plate or from defects during the plate manufacturing modifying the groove shape, as well as the neglect of viscous forces on the channel sidewalls in the model. Because the area occupied by the open or shorter channels at the tips of the plates is much smaller than the total plate area we assume that the derived expressions for the propulsion and levitation forces are valid in each channel. Strictly speaking, this is only true for infinitely long plates. Since the plates used in the experiments are of finite extension, this simplifying assumption represents a further source of error. Moreover, the plates used at low Re are equipped with tiny walls for which any manufacturing defect will have a huge impact, also possibly altering the mass distribution. At high Reynolds numbers, plates are heavy and have short channels, so that levitation becomes challenging by requiring large pressure (discussed below), which sometimes destabilises the slider and introduces further uncertainty in the measurements. This results in the increased scattering of the data at $\text{Re} \gg 1$, which complicates a quantitative comparison with the small variation of the numerical coefficients predicted by Eq. (13). However, the scaling of the propelling force (that is, how it is fixed by the plate geometry) is well captured by the data.
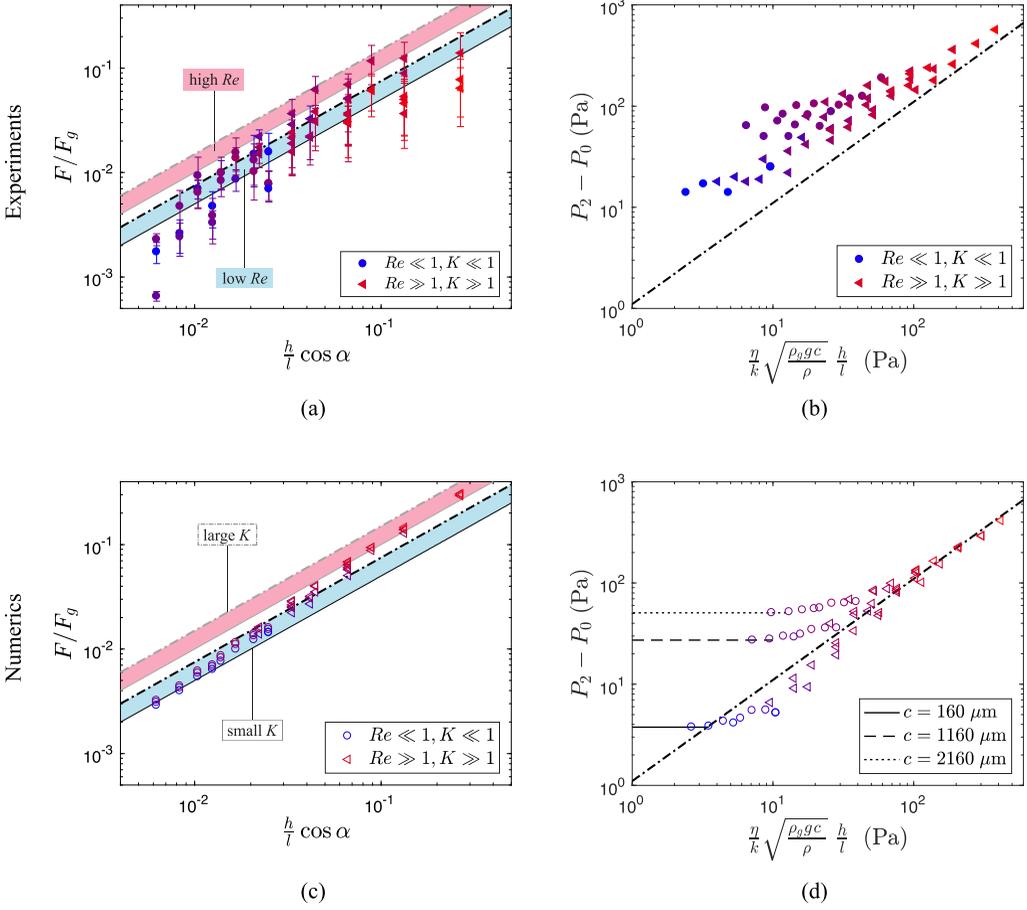
(a)

(b)

(c)

(d)

FIG. 5. (a) Ratio of the experimental total force of propulsion F to the force needed to enable levitation, F_g, as a function of the scaling factor appearing in the theoretical expression (13). The high Reynolds numbers area is colored in red, while the low Reynolds numbers area is in blue; the short channel limit is shown by the dashed lines while the long channel asymptotic case is displayed by the thin lines. The symbol shape shows the corresponding parameter K: circles ($K < 1$) and triangles ($K > 1$). Given our experimental characteristics, it varies from 0.05 to 927. The symbol color qualitatively shows the corresponding numerical Reynolds number of data, from blue (Re $\ll$ 1) to red (Re $\gg$ 1). It is found to range from 0.25 to 295. (b) Experimental pressure $P_2 - P_0$ imposed by the operator to observe levitation as function of its theoretical expression from Eq. (15c), shown by the dashed-dotted line. Symbol shapes and colors are the same as in (a). (c) Ratio of the numerical total force of propulsion F to the force needed for levitation F_g as function of the scaling factor appearing in the theoretical Eq. (13). Symbols, colors, and lines are the same as in (a). (d) Numerical pressure $P_2 - P_0$ required to induce levitation as a function of Eq. (15c), indicated by the dashed-dotted line. Horizontal lines show the long channels limit (14). Symbols, shape, and color are the same as in (a).

C. Working pressure

The working pressure P_2 chosen by the operator to induce levitation can be expressed through $P_2 - P_0 = \rho_g g c / F_g$, where ρ_g is the density of glass and F_g takes the nondimensional values described by Eqs. (9)–(12), depending on the channel geometry and the Reynolds number.

For long channels, we get to first order that the working overpressure has to compensate the pressure generated by the weight of the slide:

$$P_2 - P_0 \approx \rho_g g c, \quad \forall \text{Re} \quad \text{and} \quad K \ll 1. \tag{14}$$

For short channels, the pressure is directly proportional to K, so that P_2 quickly diverges to sustain the levitation of small objects. In the high Reynolds number regimes, the pressure is obtained using the values of K and Re from Eq. (4), and recalling that the maximal injection velocity is $v_m = \frac{k}{\eta}(P_2 - P_0)$. We get

$$\frac{P_2 - P_0}{\rho_g g c} \approx \begin{cases} \frac{K}{4}, & \text{Re} \ll 1 \ll K \\ \frac{12}{\pi^2} \frac{K}{\text{Re}} = \frac{2\sqrt{3}}{\pi} \frac{\eta}{k} \sqrt{\frac{1}{\rho \rho_g g c}} \frac{h}{l}, & 1 \ll \text{Re} \ll K. \end{cases} \tag{15}$$

It is hence challenging to obtain experimental data in the low Reynolds numbers regime, as the pressure diverges with K. In the second expression at high Reynolds numbers lower than K, we see the strong dependency of the working pressure on the plate geometry, as it is directly proportional to the slenderness $\varepsilon = h/l$ of the channel: Sliders with deep textures or short channels will require a large overpressure to levitate.

Experimental results for P_2 are compared to the laws Eqs. (14) and (15) for long and short channels in Fig. 5(b). For large overpressures (high Re and large K), experimental data show an excellent agreement with the behavior inferred from Eq. (15). For low Re and small K, however, the experimental pressure $P_2 - P_0$ is larger than the pressure generated by the slider weight, expected from Eq. (14). For short channels, most of the pressure drop happens across the porous plate, and the pressure in the channel is just above ambient (see Fig. 4): this does not provide much pressure to induce levitation, hence we experimentally need to increase P_2. Moreover, the resolution and precision of our experimental setup would not allow reaching too low airflows in a stable fashion.

D. Numerical simulations

In Sec. IV asymptotic limits for high and low Re were examined. Not all experiments fall into these limiting classes and it is desirable to extend the available results obtainable within the model of the single channel sketched in Fig. 3 to intermediate Re and channel lengths. In general, the velocity field $(u, v) = (-\psi_y, \psi_x)$ can be described by a stream function $\psi(x, y) = f(x)g(x, y)$, where $f(x)$ is the flow rate along the groove. We make the assumption that the shape of the velocity profile, encoded in $g(x, y)$, changes slowly along the channel. As described in Appendix B, using Eq. (1′) and boundary conditions Eq. (2′), we obtain two differential equations, numerically integrable for a large range of Re, allowing to solve for f and g. Results for the force of propulsion F and the working pressure P_2 are presented in Figs. 5(c) and 5(d). They show an excellent agreement with the theory, and offer a good description of the experiments, yet comparing Figs. 5(a) and 5(c) shows a slight overestimation of the experimental results by the numerical and theoretical force, as discussed above.

VI. CONCLUSION

The system described in this paper offers an easy way to transport solids, using air-blown induced levitation: propelled objects are protected against shocks and contaminations that could deteriorate them in case of contact. Propulsion is achieved using a herringbone macrotexture, but unlike previous studies [7], the texture here is directly engraved into the lower surface of the propelled solid. As air is redirected close to the object, propulsion is always observed, whatever the height of levitation [17]. The terminal velocity is not easily accessible: we suggest in the Supplemental Material [18] a detoured way to access it, exploiting rotation. The propulsion force and working pressure have been extensively discussed through a new comprehensive model, and experiments were compared to numerical results and analytical predictions. An overpressure always develops inside the channels, but the resulting propulsion can be lowered by viscous effects at low Reynolds numbers. Yet a purely viscous entrainment can only be observed if the texture is engraved on the porous substrate instead of the hovercraft, so that the inertial pressure will apply on the walls connected to the fixed box [7]. In this situation only, viscous entrainment becomes the mechanism

of propulsion. If the texture is engraved on a light slide free to move, the pressure component always dominates and propulsion happens in the direction opposite to the channeled air-flow: motion follows the tip of the herringbones. This system offers the possibility to simultaneously propel objects of various geometries at any Reynolds number and does not require specific design on the propulsion path, which facilitates applications and manipulations.

APPENDIX A: BOUNDARY LAYER ON THE TOP SURFACE FOR Re ≫ 1

The inviscid flow solution of the high Reynolds numbers case has a slip velocity $\pi/2$ on the top boundary $y = 1$. This slip calls for a boundary layer, where viscous forces are strong and the flow is slowed over a displacement thickness δ. The numerical resolution of the problem, detailed in Appendix B, shows that $\delta \sim \text{Re}^{-1/2}$. The inviscid solution applies for $0 \leqslant y \leqslant 1 - \delta$. This restriction to a slightly narrower channel makes a small change to the flow:

$$\beta^2 = \frac{\pi^2}{8} \frac{\text{Re}}{K}(1 + 2\delta), \quad \text{and} \quad g(y) \approx \cos\left(\frac{\pi}{2} \frac{y}{1 - \delta}\right).$$

Hence, the forces have a small change to

$$F_p = \begin{cases} -\frac{\pi^2}{8} \frac{\text{Re}}{K}(1 + 2\delta), & \text{short channels} \\ -1 + 2\frac{K}{\text{Re}}(1 - 2\delta), & \text{long channels} \end{cases}$$

and

$$F_g = \begin{cases} \frac{\pi^2}{12} \frac{\text{Re}}{K}(1 + 2\delta), & \text{short channels} \\ 1 - \sqrt{\frac{8}{\pi^2} \frac{K}{\text{Re}}}(1 - \delta), & \text{long channels} \end{cases}.$$

Besides, the numerical resolution gives an estimate of the shear rate at the top surface of the channel, inside the boundary layer [Eq. (B5)], leading to the scaling of the viscous force on the top surface stated in Eqs. (9) and (10).

APPENDIX B: KÁRMÁN-POHLHAUSEN APPROXIMATION

The incompressible velocity field $(u, v) = (-\psi_y, \psi_x)$ is described by a stream function ψ, which we write without loss of generality as $\psi(x, y) = f(x)g(x, y)$, where $g(x, y)$ obeys the boundary conditions

$$g(x, 0) = 1, \quad g(x, 1) = g_y(x, 0) = g_y(x, 1) = 0, \tag{B1}$$

such that $u(x, 0) = u(x, 1) = v(x, 1) = 0, v(x, 0) = f'(x)$, and $\bar{u}(x) = \int_0^1 u \, dy = f(x)$, i.e., $f'(x)$ is the scaled injection velocity and $f(x)$ the scaled average velocity (or flow rate) along the channel. $g_y(x, y)$ in turn is the normalized profile of u across the channel.

Inserting this Ansatz together with the pressure-relation Eq. (2b'), $p(x, y) \approx p(x, 0) = 1 - f'(x)$, into the x-component of the stationary Navier-Stokes Eq. (1b') and integrating over y, we obtain [using Eq. (1a') to rewrite its left-hand side as $uu_x + vu_y = 2uu_x + (uv)_y$]

$$\text{Re}\left[f^2 \int_0^1 (g_y)^2 dy\right]_x = Kf'' + (\varepsilon^2 f'' - f[g_{yy}|_{y=1} - g_{yy}|_{y=0}]). \tag{B2}$$

For known $g(x, y)$ this is the determining equation for $f(x)$ and for a suitable choice of $g(x, y)$ constitutes a Kármán-Pohlhausen approximation for the flow velocity along the channel [19]. The limiting cases studied in Sec. IV of the main text are recovered using appropriate profiles for large and small Re and omitting the viscous or inertial terms, respectively.

The splitting of the stream function $\psi(x, y)$ into an average velocity $f(x)$ and a local velocity profile $g(x, y)$ can always be made. To make progress, we need an additional assumption.
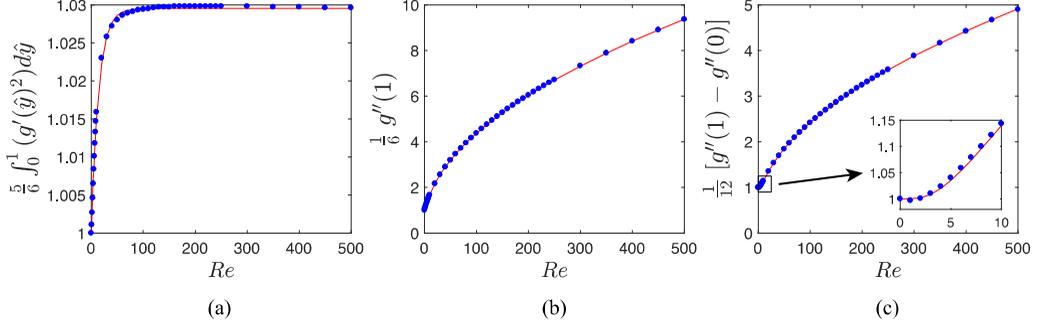
FIG. 6. The functions $(5/6)\{\int_0^1 [g'(y)]^2 dy\}$(Re) in (a), $(1/6)[g''(1)]$(Re) in (b), and $(1/12)[g''(1) - g''(0)]$(Re) in (c). Symbols are numerical values, solid lines represent the analytical approximations, Eqs. (B4)–(B6).

Specifically, we assume that the dominating x-dependence of the stream function resides in $f(x)$, such that locally, at a given position x_0, we can expand $\psi(x, y) = [f(x_0) + f'(x_0)(x - x_0)]g(x_0, y)$. Taking the y-derivative of Eq. (1b') and subtracting the x-derivative of Eq. (1c') to eliminate the pressure field, we obtain after inserting this approximate stream function

$$\partial_y[g^{(3)}(y) + \widetilde{\mathrm{Re}}[(g'(y))^2 - g(y)g''(y)]] = 0, \tag{B3}$$

where $\widetilde{\mathrm{Re}} = \mathrm{Re}\, f'(x_0)$ is the local Reynolds number based on the influx velocity and we used the abbreviation $g(y) \equiv g(x_0, y)$. Taking $\widetilde{\mathrm{Re}}$ as a parameter, Eq. (B3) can be interpreted as an ordinary differential equation for $g(y)$, numerically integrable for a large range of $\widetilde{\mathrm{Re}}$ with boundary conditions inferred from Eq. (B1).

Equation (B3) is well known from the scaling solution $\psi(x, y) = f(x)g(y)$ for constant influx into a half-open channel via one permeable wall and has been widely studied analytically for small and large Reynolds numbers [16]. Here we are interested in intermediate Reynolds numbers up to 500 such that a numerical solution lends itself. In particular, for Eq. (B2) we need approximate expressions for g'' at the channel walls, $g''(0)$ and $g''(1)$, as well as the integral of $(g')^2$ across the channel as a function of $\widetilde{\mathrm{Re}}$. Solving Eq. (B3) with $\widetilde{\mathrm{Re}}$ as parameter, we get the following best fits for $\widetilde{\mathrm{Re}} < 500$:

$$\left[\int_0^1 (g'(y))^2 dy\right](\widetilde{\mathrm{Re}}) \approx (6/5)(1 + 0.0295[1 - e^{-0.07\widetilde{\mathrm{Re}}}]), \tag{B4}$$

$$[g''(1)](\widetilde{\mathrm{Re}}) \approx 6\left[1 + \frac{0.0781\,\widetilde{\mathrm{Re}}^{1.053}}{(1 + 0.0691\,\widetilde{\mathrm{Re}})^{0.524}}\right], \tag{B5}$$

$$[g''(1) - g''(0)](\widetilde{\mathrm{Re}}) \approx 12\left[1 + \frac{0.00264\,\widetilde{\mathrm{Re}}^{7.81}}{(1 + 0.593\,\widetilde{\mathrm{Re}})^{7.24}}\right], \tag{B6}$$

where the floating-point numbers were varied to obtain least-squares fits with the corresponding fit-function. These functions are shown together with the numerical values in Fig. 6. All numerical calculations were performed using a finite-element discretization as implemented in the commercial code Comsol Multiphysics v5.0. These expressions are in agreement with exact solutions found for asymptotic regimes. For $\mathrm{Re} \to \infty$, one obtains $\int_0^1 (g'(y))^2 dy \approx \pi^2/8$ and $g''(1) \sim \mathrm{Re}^{1/2}$ [8,20,21], both agreeing suitably well with the approximate Eqs. (B5) and (B6) already. For $\mathrm{Re} = 0$, the solution is the Hagen-Poiseuille profile, for which we have $g(y) = (1 + 2y)(1 - y)^2$ and $g'(y) = -6y(1 - y)$, such that $g''(1) = -g''(0) = 6$ and $\int_0^1 (g'(y))^2 dy = 6/5$.

Finally, as evident from Fig. 6(a), the integral of the squared transverse velocity profile across the channel only changes by approximately 3% in the whole range of Re. Thus, neglecting the longitudinal derivative of this term in Eq. (B2) yields

$$\text{Re}\left[\int_0^1 (g_y)^2 dy\right](f^2)_x = Kf'' + (\varepsilon^2 f'' - f[g_{yy}|_{y=1} - g_{yy}|_{y=0}]). \tag{B2'}$$

The functionals of $g(y)$ arising in this equation can now be considered as functions of the local Reynolds number, $\widetilde{\text{Re}}$, via Eq. (B3) or their numerical approximations in Eqs. (B4)–(B6). This in turn allows us to solve Eq. (B2') numerically with the boundary conditions $f(0) = 0$ and $f'(1) = 1$. Pressures and forces are then readily obtained via Eqs. (2b') and (3') together with the scaled shear rates from Eqs. (B5) and (B6).

---

[1] E. H. Brandt, Levitation in physics, Science **243**, 349 (1989).

[2] G. Lagubeau, M. Le Merrer, C. Clanet, and D. Quéré, Leidenfrost on a ratchet, Nat. Phys. **7**, 395 (2011).

[3] E. H. Brandt, Acoustic physics: Suspended by sound, Nature **413**, 474 (2001).

[4] F. C. Moon, *Superconducting Levitation: Applications to Bearing and Magnetic Transportation* (John Wiley & Sons, New York, 2008).

[5] A. Ashkin and J. M. Dziedzic, Optical levitation by radiation pressure, Appl. Phys. Lett. **19**, 283 (1971).

[6] G. J. Laurent, A. Delettre, and N. Le Fort-Piat, A new aerodynamic-traction principle for handling products on an air cushion, IEEE Trans. Robotics **27**, 379 (2011).

[7] D. Soto, H. de Maleprade, C. Clanet, and D. Quéré, Air-levitated platelets: From take-off to motion, J. Fluid Mech. **814**, 535 (2017).

[8] E. J. Hinch and J. Lemaitre, The effect of viscosity on the height of disks floating above an air table, J. Fluid Mech. **273**, 313 (1994).

[9] J. R. Lister, A. B. Thompson, A. Perriot and L. Duchemin, Shape and stability of axisymmetric levitated viscous drops, J. Fluid Mech. **617**, 167 (2008).

[10] H. Boerhaave, *Elementa Chemiae* (Lugduni Batavorum, Leiden, 1732), Vol. 1.

[11] J. G. Leidenfrost, On the fixation of water in diverse fire, Int. J. Heat Mass Transf. **9**, 1153 (1966).

[12] H. Linke, B. J. Alemán, L. D. Melling, M. J. Taormina, M. J. Francis, C. C. Dow-Hygelund, V. Narayanan, R. P. Taylor, and A. Stout, Self-Propelled Leidenfrost Droplets, Phys. Rev. Lett. **96**, 154502 (2006).

[13] T. Baier, G. Dupeux, S. Herbert, S. Hardt, and D. Quéré, Propulsion mechanisms for Leidenfrost solids on ratchets, Phys. Rev. E **87**, 021001 (2013).

[14] D. Soto, G. Lagubeau, C. Clanet, and D. Quéré, Surfing on a herringbone, Phys. Rev. Fluids **1**, 013902 (2016).

[15] M. A. Goldshtik, V. M. Khanin, and V. G. Ligai, A liquid drop on an air cushion as an analogue of Leidenfrost boiling, J. Fluid Mech. **166**, 1 (1986).

[16] G. Leal, *Advanced Transport Phenomena: Fluid Mechanics and Convective Transport Processes* (Cambridge University Press, Cambridge, 2007).

[17] A. D. Fitt, G. Kozyreff, and J. R. Ockendon, Inertial levitation, J. Fluid Mech. **508**, 165 (2004).

[18] See Supplemental Material at http://link.aps.org/supplemental/10.1103/PhysRevFluids.3.104101 for details on platelet manufacture and rotational propulsion of textured platelets as well as videos of both linear and rotational motion.

[19] J. Hartwig and S. Darr, Analytical model for steady flow through a finite channel with one porous wall with arbitrary variable suction or injection, Phys. Fluids **26**, 123603 (2014).

[20] F. Skalak and C.-Y. Wang, Fluid dynamics of a long porous slider, J. Appl. Mech. **42**, 893 (1975).

[21] C. Y. Wang, A porous slider with velocity slip, Fluid Dyn. Res. **44**, 065505 (2012).